Article

High-Temperature Oxidation of Boiler Steels at 650 °C

Jaka Burja , Barbara Šetina Batič , Borut Žužek , Tilen Balaško *

Posted Date: 20 September 2023

doi: 10.20944/preprints202309.1268.v1

Keywords: high-temperature oxidation; thermogravimetric analysis; kinetics; CALPHAD; boiler steels; SEM; EBSD

Article

High-Temperature Oxidation of Boiler Steels at 650 °C

Jaka Burja [1,2], Barbara Šetina Batič [2], Borut Žužek [2] and Tilen Balaško [1,*]

[1] Faculty of natural sciences and engineering, University of Ljubljana, Aškerčeva cesta 12, 1000 Ljubljana, Slovenia

[2] Institute of metals and technology, Lepi pot 11, 1000 Ljubljana, Slovenia

* Correspondence: tilen.balasko@ntf.uni-lj.si; Tel.: +38612000457

Abstract: This study presents a comprehensive investigation of the formation, composition, and behaviour of oxide layers during the high-temperature oxidation of four different steel alloys (16Mo3, 13Cr, T24 and P91) at a uniform temperature of 650 °C. The research combines CALPHAD (CALculation of PHAse Diagrams) calculations, thermogravimetric analysis (TGA) and advanced microscopy techniques, including scanning electron microscopy (SEM) and electron backscatter diffraction (EBSD), to elucidate the complex mechanisms controlling oxidation kinetics and oxide layer development. CALPHAD calculations were used to determine the thermodynamically stable phases for each steel type at 650 °C. The results showed different phase compositions, highlighting the importance of steel composition in the formation of oxide layers. Each steel grade exhibited different kinetics, with 16Mo3 steel showing the highest oxidation rate, followed by 13Cr, T24 and P91. This variability highlights the role of steel composition, particularly chromium content, in determining oxidation behaviour. These results have significant implications for temporary overheating in industrial applications and contribute to a deeper understanding of oxidation processes in steels.

Keywords: high-temperature oxidation; thermogravimetric analysis; kinetics; CALPHAD; boiler steels; SEM; EBSD

1. Introduction

Operating temperatures of 600 °C are typical for the energy industry, they are called elevated temperatures. Steels used at elevated temperatures must retain their properties. Unlike conventional steels used at room temperature, such as spring and structural steels, boiler steels must withstand the high temperatures under stress loading and oxidation. They must be resistant to hot gases and corrosion, have sufficient strength at high temperatures and creep deformation, and be easily weldable [1–4].

Even unheated areas in heating and reheat tubes of utility steam generators are exposed to harsh oxidation conditions. The inner surfaces are exposed to high-temperature steam, while the outer surfaces are exposed to high-temperature air. The higher the steam temperature, the better the efficiency of the plant. The steel components are designed to operate for 100 000 hours. In practise, temporary local overheating can occur, which deteriorates the material. Therefore, it is important to assess the damage of such temporary thermal loads [1,5,6]. The aim of this study is to demonstrate the oxidation resistance at 600 °C of steels commonly used for such components.

The most important alloying elements for steels used at elevated temperatures are chromium – Cr, vanadium – V and molybdenum – Mo. Chromium is the most important element for corrosion resistance and therefore protects the component from severe oxidation at higher operating temperatures. The carbon content of the different boiler steel grades is comparable. Yield strength and tensile strength do not differ significantly, as they are most influenced by carbon. Here, the already mentioned carbide-forming elements (Cr, Mo, V) as well as tungsten – W, niobium – Nb and titanium - Ti contribute to increasing the creep resistance [6–8].

 doi:10.20944/preprints202309.1268.v1

16Mo3, 13CrMo4-5, T24 and P91 are steel grades commonly used in energy production. These steels are widely used in power plants and other energy-related applications due to their specific properties that make them suitable for high-temperature and high-pressure environments.

16Mo3 is a low-alloy steel used in power plant equipment such as boilers and pressure vessels. It is designed to withstand high temperatures, have good creep resistance and is easy to weld. Small amounts of molybdenum (up to 0.35 wt.%) and chromium (up to 0.3 wt.%) provide heat resistance [9].

13Cr (13CrMo4-5) is a higher alloyed steel that contains up to 1 wt.% Cr and up to 0.6 wt.% Mo compared to 16Mo3 and has better oxidation and creep resistance [10].

T24, also known as 7CrWVMoNb9-6, is a high-temperature steel often used for the construction of superheaters and reheaters in power plants. It belongs to the group of so-called advanced ultra-supercritical (A-USC) steels, which are designed for extremely high temperatures and pressures. T24 contains chromium (up to 2.6 wt.%), molybdenum (up to 1.1 wt.%) and vanadium and niobium as important alloying elements that provide creep strength, oxidation resistance and thermal stability [11].

P91, or 9Cr-1Mo-V steel, is used extensively for the construction of boilers, steam pipes and other components in power plants. Thanks to the numerous carbide-forming elements, which include V and Nb in addition to Cr and Mo, it has a high creep resistance. In addition, P91 contains 0.03 to 0.07 wt.% N forming MX carbon nitrides, which provide excellent creep resistance. Oxidation resistance at elevated temperatures is provided by the high Cr content (up to 9.5 wt.%), making it suitable for long-term use in demanding conditions [12–14].

In summary, these steels play a crucial role in energy production, each offering specific advantages for different applications.

2. Materials and Methods

The chemical compositions of studied steels given in Table 1 were investigated by wet chemical analysis and infrared absorption after combustion with ELTRA CS-800.

Table 1. The chemical composition of the steels examined is given in percentages by weight.

Sample	C	Si	Mn	P	S	Cr	Ni	Mo	Nb	V	Fe
16Mo3	0.2	0.35	0.9	0.005	0.001	0.3	0.3	0.35	/	/	Bal.
13Cr	0.17	0.35	0.7	0.004	0.001	1.15	0.3	0.6	/	/	Bal.
T24	0.1	0.45	0.7	0.004	0.002	2.6	/	1.1	/	0.3	Bal.
P91	0.12	0.5	0.6	0.003	0.001	9.5	0.4	1.05	0.1	0.25	Bal.

To obtain a preliminary understanding of the composition of the oxide layers, we conducted CALPHAD (CALculation of PHAse Diagrams) calculations using the software Thermo-Calc (Thermo-Calc 2020a, Thermo-Calc Software AB, Stockholm, Sweden) and the thermodynamic database TCOX9 [15] (Metal Oxide Solutions Database). In the diagrams the amount of phase is shown on the Y-axis and the activity of O_2 is shown on X-axis. The calculations were focused at determining the composition of the oxide layers formed at an oxidation temperature of 650 °C.

The high-temperature oxidation process was studied at 650 °C in an air atmosphere for 24 hours. The samples for metallographic analysis were oxidised in a Bähr DL 805A/D quench dilatometer (TA Instruments, New Castle DE, USA), which allowed rapid cooling rates. This preserved the scale structures formed at temperatures above 570 °C and prevented oxidation or decomposition of the wüstite during cooling. The samples were heated at a rate of 10 °C min^{-1}, while the cooling rate was 30 °C s^{-1}, to preserve the oxide layers formed. To improve the oxidation conditions, additional air (79 vol.% nitrogen, 21 vol.% oxygen, 0.9 vol.% argon and 0.1 vol.% of hydrocarbons and other inert gases) was introduced into the furnace at a flow rate of 0.3 L min^{-1}.

The samples used for the study of kinetics were oxidised in the NETZSCH STA Jupiter 449C (NETZSCH Holding, Selb, Germany) machine. The heating and cooling rate was 10 °C min^{-1}, in addition air was blown into the furnace at a flow rate of 30 mL min^{-1} (during the heating/cooling and

Preprints (www.preprints.org) | NOT PEER-REVIEWED | Posted: 20 September 2023 doi:10.20944/preprints202309.1268.v1

the isothermal section). Thermogravimetric Analysis (TGA) was used to study the kinetics, with the samples placed on an alumina slip-on plate coated with a 1-mm thick platinum layer. Once the experiment was completed, the TGA data was exported, and the weight gain on the specific surface was calculated. A graph was then generated using OriginPro (OriginLab Corporation, Northampton MA, USA) software, version 2016.

The samples were ground and polished before SEM analysis. The composition and thickness of the oxide layers were examined using a ZEISS CrossBeam 550 (Carl Zeiss AG, Oberkochen, Germany) instrument. EDS (Energy-Dispersive X-ray Spectroscopy) and EBSD (Electron Backscatter Diffraction) analyses were performed with a HikariSuper EBSD camera (EDAX, Mahwah NJ, USA), to investigate the composition of the oxide layers formed.

3. Results and Discussion

3.1. CALPHAD calculations

The content of thermodynamically stable phases as a function of oxygen activity (a_O) for all investigated steel grades at 650 °C is shown in Figures 1–4. Figure 1 shows the results for the steel 16Mo3. According to this at 650 °C up to $a_O \approx 10^{-13}$, the stable oxide $(Fe, Cr)_2O_3$ (95.9 wt.%) predominates, followed by $(Fe, Mn)_2SiO_4$ (2.8 wt.%) and the remaining 1.3 wt.% is $(Fe, Cr, Mn, Mo)_3O_4$. In the range $a_O \approx 10^{-13}$–10^{-23}, $(Fe, Cr, Mn, Mo)_3O_4$ is stable and predominant (96.7 wt.%), followed by $(Fe, Mn)_2SiO_4$ (3.3 wt.%) and in the range $a_O \approx 10^{-22}$–10^{-23} (Fe, Mn, Ni)O (the content increases to 90.7 wt.%) and the rest is $(Fe, Cr, Mn, Mo)_3O_4$ and $(Fe, Mn)_2SiO_4$ (but the content of these two changes with a_O according to the wüstite content). It is also observed that internal oxidation occurs at 650 °C, so that $(Fe, Cr, Mn, Mo)_3O_4$ and $(Fe, Mn)_2SiO_4$ are stable under the steel surface. In all cases, internal oxidation was determined by the amount of α-ferrite phase, as the α-ferrite content calculated at equilibrium at a temperature of 650 °C is 97.5 wt.%. Therefore, we can determine whether internal oxidation takes place or not. If the α-ferrite content increases (black line), it should immediately increase to 97.5 wt.%, if not, internal oxidation takes place, as shown in Figure 1.

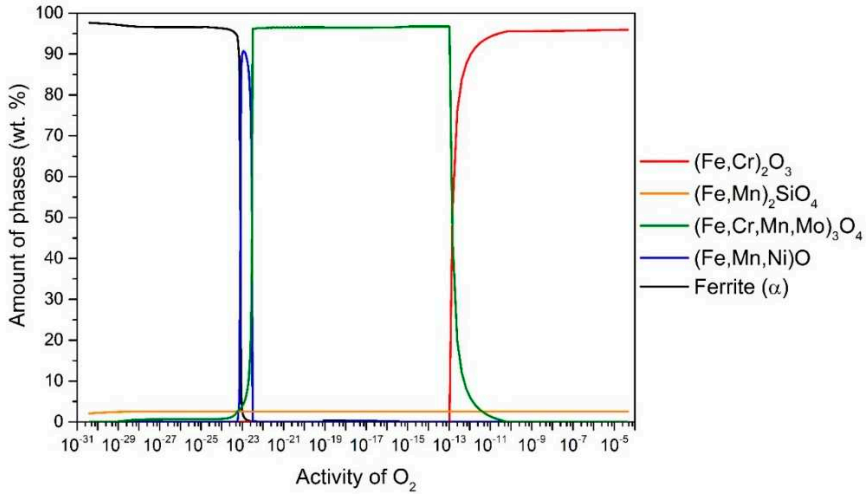

Figure 1. The amount of thermodynamically stable phases formed during high-temperature oxidation as a function of oxygen activity for 16Mo3 steel at 650 °C.

Figure 2 shows the results for 13Cr steel. Thus at 650 °C up to $a_O \approx 10^{-13}$, the stable oxide $(Fe, Cr, Mn)_2O_3$ (95.6 wt.%) predominates, followed by Fe_2SiO_4 (4.4 wt.%). In the range $a_O \approx 10^{-13}$–10^{-22}, $(Fe, Cr, Mn, Mo)_3O_4$ is stable and predominant (96.7 wt.%), followed by Fe_2SiO_4 (3.3 wt.%) and in the range $a_O \approx 10^{-22}$–10^{-23} (Fe, Mn, Ni)O (the content of which increases up to 83 wt.%) and the remainder is $(Fe, Cr, Mn, Mo)_3O_4$ and Fe_2SiO_4 (but the content of these two changes with a_O according to the wüstite content). It is also observed that internal oxidation occurs at 650 °C, so that $(Fe, Cr, Mn, Mo)_3O_4$ and Fe_2SiO_4 are stable under the steel surface. In all cases, the internal oxidation was determined by the

Preprints (www.preprints.org) | NOT PEER-REVIEWED | Posted: 20 September 2023 doi:10.20944/preprints202309.1268.v1

amount of α-ferrite phase, as the equilibrium calculated α-ferrite content at 650 °C is 97 wt.%. Therefore, we can determine whether internal oxidation occurs or not. If the α-ferrite content increases (black line), it should immediately increase to 97 wt.%. If not, internal oxidation takes place, as shown in Figure 2.

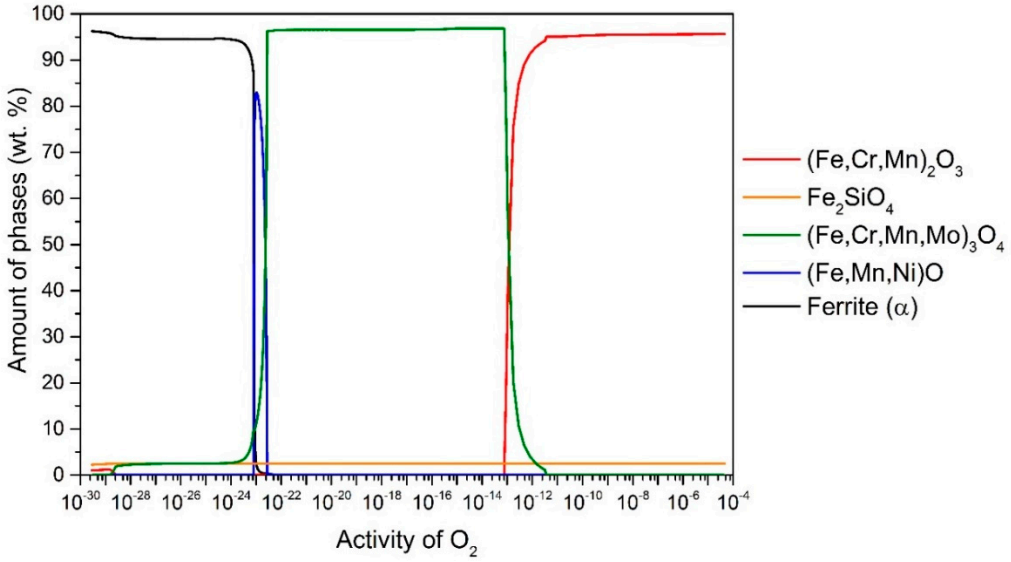

Figure 2. The amount of thermodynamically stable phases formed during high-temperature oxidation as a function of oxygen activity for 13Cr steel at 650 °C.

Figure 3 shows the results for T24 steel. At 650 °C up to $a_O \approx 10^{-13}$, the stable oxide $(Fe, Cr, V)_2O_3$ (94.3 wt.%) predominates, followed by $(Fe, Mn)_2SiO_4$ (5.7 wt.%). In the range $a_O \approx 10^{-13}$–10^{-22}, $(Fe, Mo, Mn, Cr)_3O_4$ is stable and predominant (96.7 wt.%), followed by $(Fe, Mn)_2SiO_4$ (3.3 wt.%) and in the range $a_O \approx 10^{-22}$–10^{-23} (Fe, Cr, V)O (the content of which increases up to 76.4 wt.%) and the rest is $(Fe, Mo, Mn, Cr)_3O_4$ and $(Fe, Mn)_2SiO_4$ (but the content of these two changes with a_O according to the wüstite content). It is also observed that internal oxidation occurs at 650 °C, so that $(Fe, Mo, Mn, Cr)_3O_4$, $(Fe, Mn)_2SiO_4$ and $(Fe, Cr, V)_2O_3$ are stable under the steel surface. In all cases, internal oxidation was determined by the amount of α-ferrite phase, as the equilibrium calculated α-ferrite content at the temperature of 650 °C is 98.5 wt.%. Therefore, we can determine whether internal oxidation occurs or not. If the α-ferrite content increases (black line), it should immediately increase to 98.5 wt.%, otherwise, internal oxidation occurs, as shown in Figure 3.

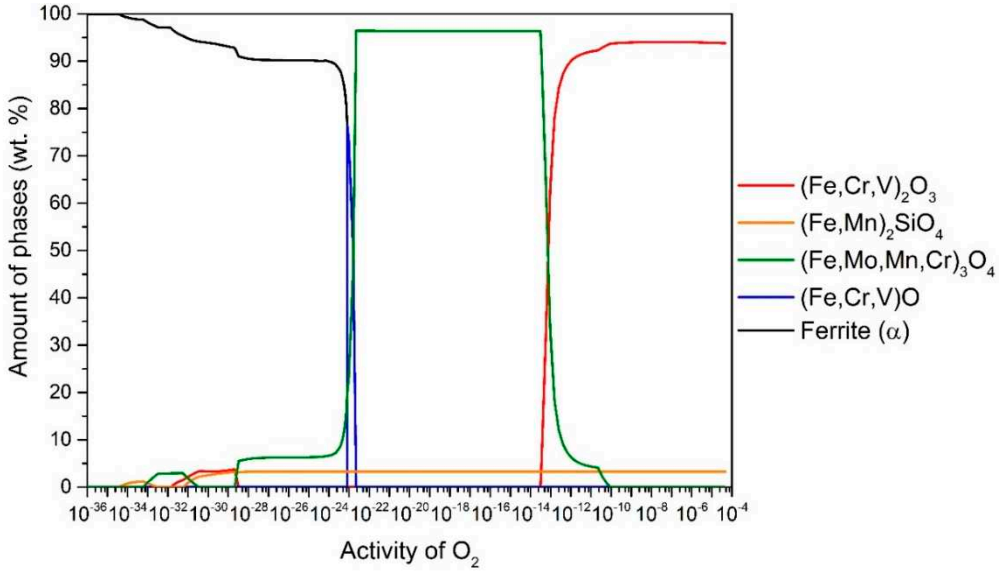

Preprints (www.preprints.org) | NOT PEER-REVIEWED | Posted: 20 September 2023 doi:10.20944/preprints202309.1268.v1

Figure 3. The amount of thermodynamically stable phases formed during high-temperature oxidation as a function of oxygen activity for T24 steel at 650 °C.

Figure 4 shows the results for the steel P91. According to this at 650 °C up to $a_O \approx 10^{-14}$, the stable oxide $(Cr, V)_2O_3$ (94.2 wt.%) predominates, followed by $(Fe, Cr)_2SiO_4$ (5.8 wt.%). In the range $a_O \approx 10^{-14}$–10^{-22}, $(Cr, Mn, V, Fe)_3O_4$ is stable and predominant (96.1 wt.%), followed by $(Fe, Cr)_2SiO_4$ (3.9 wt.%) and in the range $a_O \approx 10^{-23}$–10^{-24} (Fe, Cr, V, Mn)O (the content of which increases up to 45.8 wt.%) and the rest is $(Cr, Mn, V, Fe)_3O_4$ and $(Fe, Cr)_2SiO_4$ (but the content of these two changes with a_O according to the wüstite content). It is also observed that internal oxidation occurs at 650 °C, so that $(Cr, Mn, V, Fe)_3O_4$, $(Fe, Cr)_2SiO_4$ and $(Cr, V)_2O_3$ are stable under the steel surface. In all cases, internal oxidation was determined by the amount of α-ferrite phase, as the equilibrium calculated α-ferrite content at the temperature of 650 °C is 97.8 wt.%. Therefore, we can determine whether internal oxidation occurs or not. If the α-ferrite content increases (black line), it should immediately increase to 97.8 wt.%, otherwise, internal oxidation occurs, as shown in Figure 4.

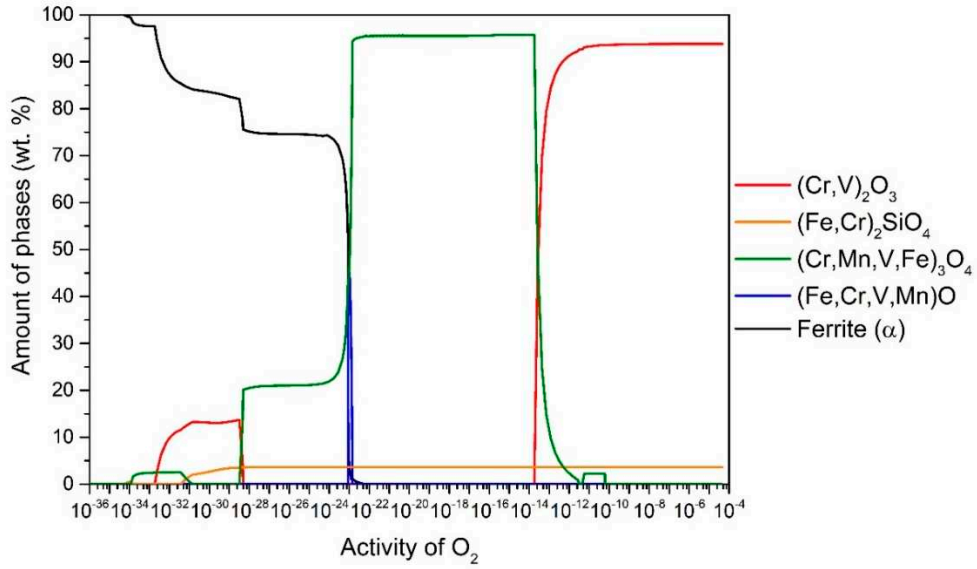

Figure 4. The amount of thermodynamically stable phases formed during high-temperature oxidation as a function of oxygen activity for P91 steel at 650 °C.

3.2. Thermogravimetric analysis

Thermogravimetric analysis (TGA) was used to measure the change in weight of the steels studied during high-temperature oxidation, as this is the most common method for studying the oxidation rate and can be measured continuously or discontinuously [16]. An iterative rectangular distance regression algorithm was used for the best fit of the TGA results to the mathematical functions. A two-phase exponential growth function (equations (1)), a second-degree polynomial (equation (2) - parabolic law) and a third-degree polynomial (equation (3) - cubic law) were used to describe the curves (TGA results).

$$W\left(\frac{\Delta m}{A}\right) = y = Ae^{\left(\frac{t}{B}\right)} + Ce^{\left(\frac{t}{D}\right)} + E \quad (1)$$

$$W\left(\frac{\Delta m}{A}\right) = y = Ae^{\left(\frac{t}{B}\right)} + E \quad (2)$$

$$W\left(\frac{\Delta m}{A}\right) = y = A + Bt + Ct^2 \quad (3)$$

Preprints (www.preprints.org) | NOT PEER-REVIEWED | Posted: 20 September 2023 doi:10.20944/preprints202309.1268.v1

In all cases, t is the time in s, Δm is the change in weight in mg, A is the specific surface area of the sample in cm^2, while the other coefficients depend on the temperature and the chemical composition of the steel.

However, since oxidation kinetics is usually studied by a change in mass as a function of oxidation time, a parabolic law can be expressed by the Pilling-Bedworth equation [17,18]:

$$dW/dt = k_p'W \quad \text{ali} \quad W^2 = k_p t + W_0^2 \tag{4}$$

Where W is the change in mass per unit area due to oxidation of iron and k_p ($=2k_p'$) is the parabolic constant in $g^2\ cm^{-4}\ sec^{-1}$, and W_0 is the initial mass at the time (t = 0) of parabolic oxidation. In the original Pilling-Bedworth equation [18], W_0 is equal to 0. The most suitable method to obtain the equation for calculating the rate constant for the oxidation of steel during continuous heating or cooling was developed by Kofstad [19]. According to his interpretation, oxidation following a linear, parabolic, or cubic law can be generally expressed as follows:

$$W^{n-1}[dW/dt] = k_n \tag{5}$$

where W is defined as the change in mass per unit area over time t, n is a constant with values of 1, 2, or 3 for the linear, parabolic, or cubic law, and k_n is a time-independent rate constant expressed as:

$$k_n = B\ exp(-Q/RT) \tag{6}$$

Where B is the constant, T is the absolute temperature, R is the gas constant, and Q is the activation energy.

The rate constants were calculated for all samples studied after equation (5) was derived by simple linear regression. The basic equation for the calculation of the rate constant (k_n) is as follows:

$$\left(\frac{\Delta m}{A}\right)^n = k_n t \tag{7}$$

Where Δm is the change in weight in mg, A is the specific surface area in cm^2, t is the oxidation time in s, and k_n is the rate constant, where n can be 1, 2, or 3, respectively, in the case of a linear, parabolic, or cubic law. In the case of the exponential law, $1 < n < 3$. The index n was named after the type of equation, so that the exponential law has the index e and the cubic law the index c.

The following graph (Figure 5) shows the TGA results of the steels examined. After 4 hours, the oxidation kinetics of steel 16Mo3 starts to follow a parabolic law and the TGA results can be expressed with a parabolic equation, but overall, the best fit is still the exponential equation. For steel 13Cr, the same trend is observed but it seems to be faster as the oxidation kinetics starts to follow a parabolic law after 2 hours. On the other hand, the oxidation kinetics of steel T24 follows the cubic law. The oxidation kinetics of steel P91 can be described by the cubic law, as the TGA results agree best with the cubic equation. In a study on the high-temperature oxidation behaviour of P91 steel [20], it was suggested that it follows a parabolic law (at 600 °C and 700 °C). We cannot confirm this, but on the other hand its oxidation time was 1000 hours. We assume that this is the same trend as for the 16Mo3 and 13Cr steels in this study.

Preprints (www.preprints.org) | NOT PEER-REVIEWED | Posted: 20 September 2023 doi:10.20944/preprints202309.1268.v1

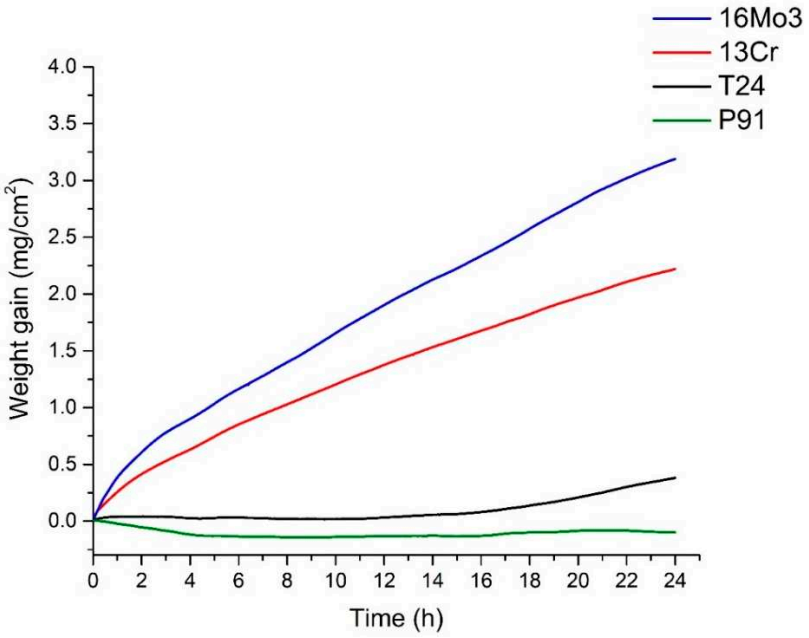

Figure 5. TGA results of the investigated steels.

The equation types with the corresponding coefficients that best fit the TGA results are listed in Table 2.

Table 2. Equation types with corresponding coefficients are given for the TGA results of the steels investigated.

Steel type	Equation type	Coefficients				
		A	B	C	D	E
16Mo3	exponential	-0.39432	-0.91794	-13.35091	-100.58937	13.73932
13Cr	exponential	-0.20042	-1.22558	-4.61321	-42.56005	4.85056
T24	cubic	0.03753	$-1.75842 \cdot 10^{-4}$	$-6.89547 \cdot 10^{-4}$	$5.55997 \cdot 10^{-5}$	
P91	cubic	0.00894	-0.03923	0.003	$-6.4608 \cdot 10^{-5}$	

The calculated results of the rate constants are shown in Table 3. The results of the rate constants are a clear indication that the oxidation kinetics is fastest for 13Cr steel, followed by 16Mo3, T24 and P91. This means that 13Cr steel oxidises the most and P91 the least.

Table 3. The rate constants of the steels examined with the corresponding equation types.

Steel type	Equation type	Rate constants	
		k_e ($mg^e\ cm^{-2e}\ s^{-1}$)	k_c ($mg^3\ cm^{-6}\ s^{-1}$)
16Mo3	exponential	$2.706 \cdot 10^{-4}$	/
13Cr	exponential	$1.028 \cdot 10^{-4}$	/
T24	cubic	/	$3.120 \cdot 10^{-7}$
P91	cubic	/	$4.893 \cdot 10^{-9}$

3.3. Microscopy

The oxide layers formed were further analysed using SEM (Figure 6). It can be seen that the thickest oxide layer was formed on steel 16Mo3, followed by 13 Cr, T24 and P91. The results are in agreement with the analysis of TG (Figure 5) and consequently with the calculated rate constants (Table 3).

Preprints (www.preprints.org) | NOT PEER-REVIEWED | Posted: 20 September 2023 doi:10.20944/preprints202309.1268.v1

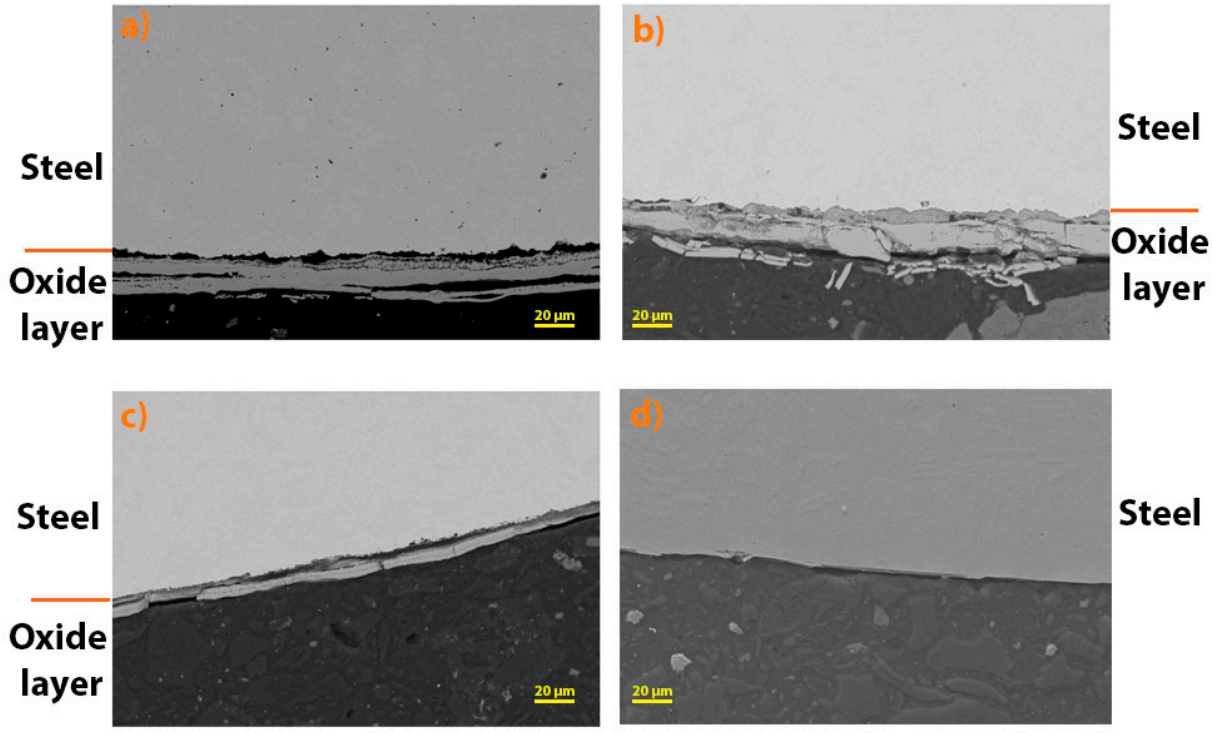

Figure 6. Oxide layers formed after high-temperature oxidation at 650 °C for (**a**) 16Mo3, (**b**) 13Cr, (**c**) T24 and (**d**) P91 steel.

In addition, the thickness of the oxide layers formed on the steels examined was measured. The following table (Table 4) shows the average of the measured thickness. The results show that the thickest oxide layer was formed on 13Cr steel, followed by 16Mo3, T24 and P91 (with no oxide layer observed on SEM). For 13Cr steel, there are deviations from the TG analysis results, but if you look at Figure 6, it is obvious that the oxide layer on 13Cr steel is cracked and chipped, which is why these results differ. And as already mentioned, no oxide layer was found on the surface of P91 steel after high-temperature oxidation, which is also in agreement with the results of the TG analysis (Figure 5).

Table 4. Thickness of the oxide layers formed on the steels examined.

Steel type	Thickness of oxide layer [µm]
16Mo3	22
13Cr	30
T24	7
P91	/

The oxide layers formed were also examined using EBSD analysis. Figure 7 shows the oxide layer formed after high-temperature oxidation of 16Mo3 steel. It is obvious that the outer and middle oxide layers consist mainly of hematite. On the other hand, the inner oxide sublayer is mainly magnetite. IPF-Z mapping also showed that the grain size in the outer and inner oxide layers is smaller than in the middle oxide sublayer. However, EDS analysis showed no differences within the oxide layer. Fe, O and Cr are essentially homogeneously distributed throughout the oxide layer formed. There are some green coloured grains in the oxide layer (mainly in the middle and inner oxide sublayers), which are not ferrite but wüstite, as both have the same body-centered cubic crystal structure (bcc). This applies to all oxide layers of the examined samples (Figures 7–10), i.e., green coloured grains in the oxide layer are wüstite and not ferrite.

Preprints (www.preprints.org) | NOT PEER-REVIEWED | Posted: 20 September 2023 doi:10.20944/preprints202309.1268.v1

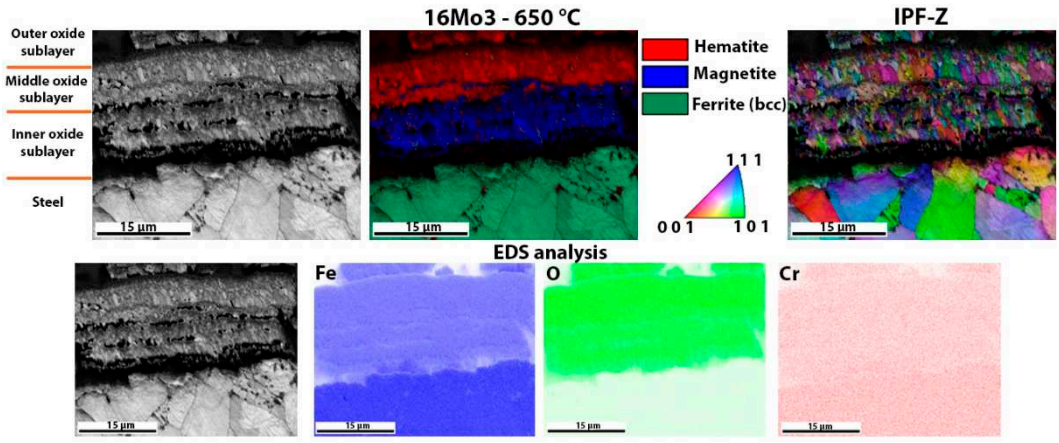

Figure 7. Detailed analysis of the oxide layer of 16Mo3 steel after high-temperature oxidation, EBSD phase analysis, the crystal orientations and EDS analysis of the surface distribution of the elements in the oxide layer formed.

Figure 8 shows the oxide layer formed after high-temperature oxidation of 13Cr steel. It is obvious that the outer and inner oxide sublayer consists mainly of hematite. On the other hand, the inner oxide sublayer is mainly magnetite. IPF-Z mapping also shows that the grain size in the outer and inner oxide sublayer is smaller than in the middle oxide sublayer. The EDS analysis of the surface distribution of the elements shows that there is an increased Cr content in the inner oxide sublayer. However, as far as O and Fe are concerned, they are essentially homogeneously distributed throughout the oxide layer formed. In the oxide layer (mainly in the middle and inner oxide sublayers) there are some green coloured grains which are not ferrite but wüstite, as both have the same body centered cubic crystal structure (bcc). In this case, there are fewer wüstite crystal grains in the oxide layer than in the 16Mo3 steel. This is also consistent with the results of the TG analysis (Figure 5), as diffusion is fastest in the wüstite, which means that the oxidation rate should be higher for 16Mo3 steel than for 13Cr and the calculated rate constant (Table 3) should also be lower than that calculated for 16Mo3 steel.

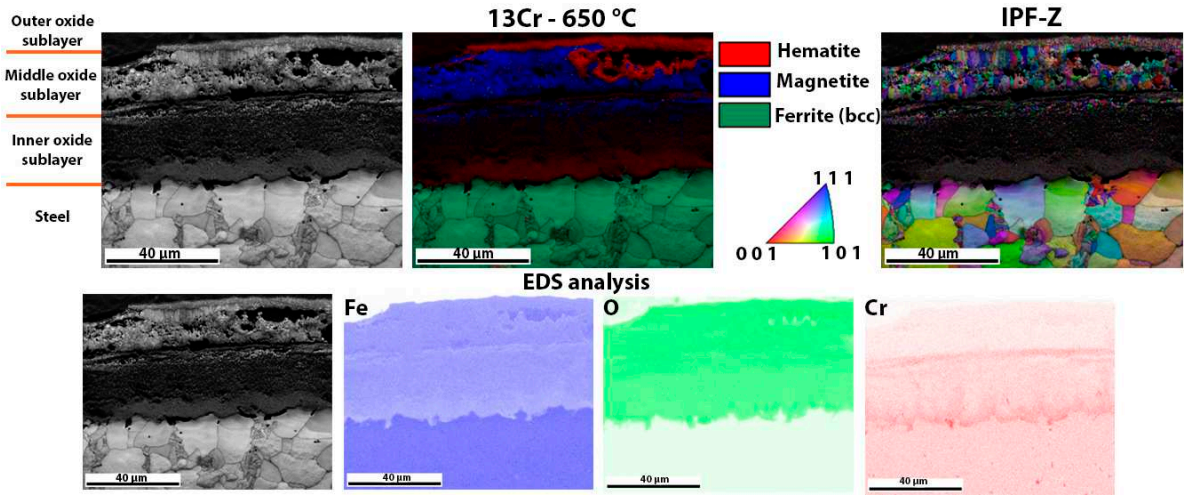

Figure 8. Detailed analysis of the oxide layer of 13Cr steel after high-temperature oxidation, EBSD phase analysis, the crystal orientations and EDS analysis of the surface distribution of the elements in the oxide layer formed.

The last oxide layer analysed was one that had formed on T24 steel after high-temperature oxidation (Figure 9). In this case, although an oxidation layer was found, the entire sublayer consisted

Preprints (www.preprints.org) | NOT PEER-REVIEWED | Posted: 20 September 2023 doi:10.20944/preprints202309.1268.v1

mainly of hematite. Some magnetite crystal grains were found in the inner oxide sublayer and some wüstite grains were also found in the middle oxide sublayer. As far as the size of the grains is concerned, the same trend as in the other analysed oxide layers is shown, i.e., the outer and inner oxide sublayers consist of smaller crystal grains than the inner oxide sublayer. EDS analysis of the surface distribution of the elements shows that the Cr content is increased in the inner oxide sublayer, while the Fe content decreases in the inner oxide sublayer. O, on the other hand, is essentially homogeneously distributed over the entire oxide layer formed. The results again agree well with the analytical results from TG (Figure 5), where T24 steel shows the second lowest weight increase during high-temperature oxidation and the second lowest calculated rate constant (Table 3).

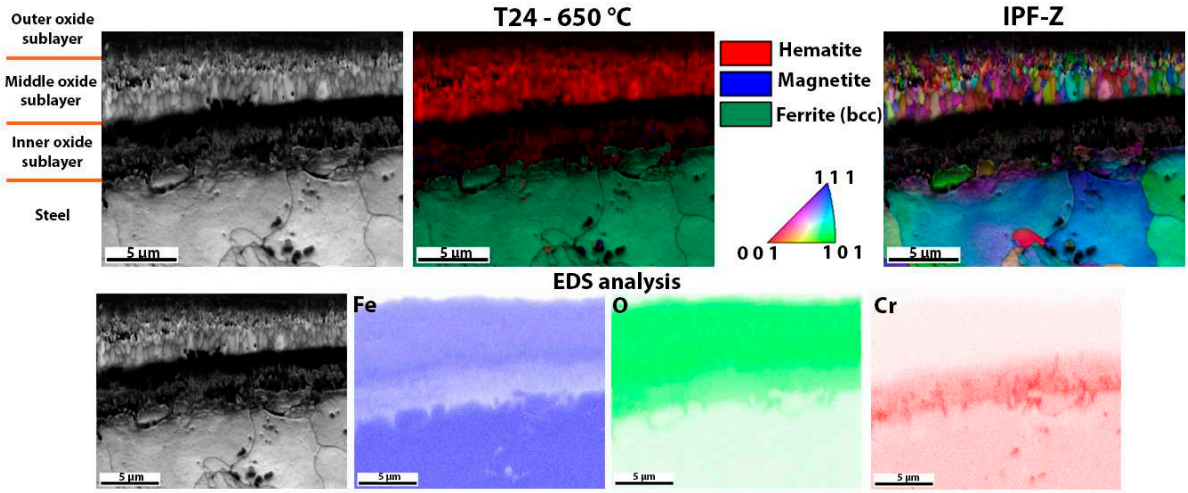

Figure 9. Detailed analysis of the oxide layer of T24 steel after high-temperature oxidation, EBSD phase analysis, the crystal orientations and EDS analysis of the surface distribution of the elements in the oxide layer formed.

Figure 10 shows the surface of P91 steel after high-temperature oxidation. In this case, there was no oxide layer that could be analysed with EBSD. The result was to be expected as the TG analysis also showed that there was only a minimal increase in weight during oxidation. EDS analysis was also only done to show that there is no oxide layer that can be analysed (there is no increased amount of oxygen on the steel surface), it only shows that there are some Cr-based carbides in the matrix (areas with increased Cr). This is also consistent with the results of the TG analysis (Figure 5), as P91 steel has the lowest weight increase during high-temperature oxidation and the lowest calculated rate constant (Table 3).

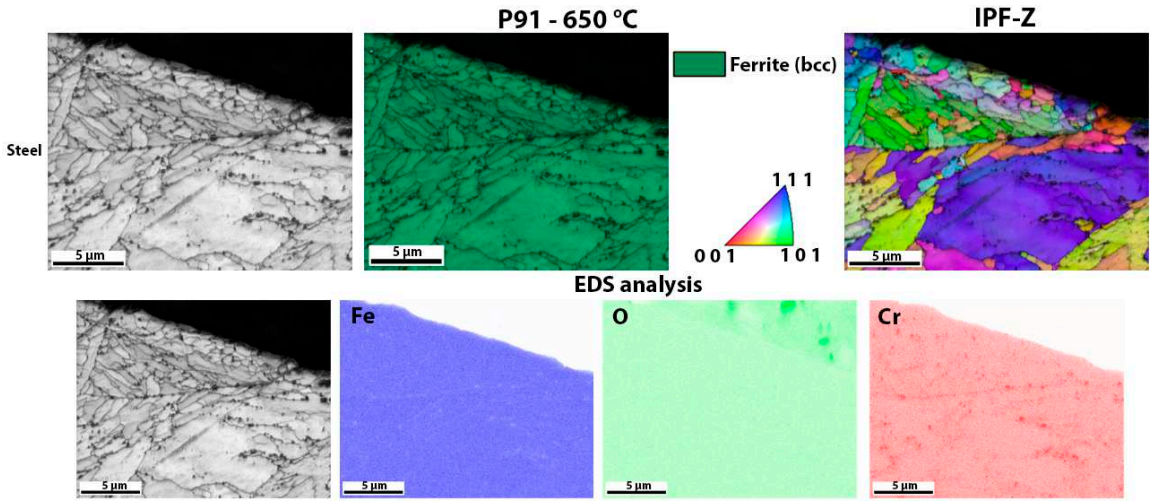

 doi:10.20944/preprints202309.1268.v1

Figure 10. Detailed analysis of the surface of P91 steel after high-temperature oxidation, EBSD phase analysis, the crystal orientations and EDS analysis of the surface distribution of the elements.

The Cr content is the decisive factor in high-temperature oxidation. Even an average content of 2.6 wt.% lowers the oxidation rate considerably (as can be seen in Table 3), the Cr content also changes the oxidation curve from exponential to cubic. This means that steels with low Cr content such as 16Mo3 and 13Cr are susceptible to severe oxidation, even in the presence of short-term, transient overheating. The strong weight gain due to oxidation is already visible after one hour (see Figure 5). The thicker oxide layers in the 16Mo3 and 13Cr steels show a clear distinction between hematite and magnetite, as shown by the EBSD analysis in Figures 7 and 8. At higher Cr contents, such as in steel T24, magnetite should form, but the crystal structure is difficult to assess with EBSD due to the smaller grain size, so only the Fe-rich hematite can be clearly distinguished. The high Cr contents in P91 prevent a much thicker oxide layer formation, so that the oxide layer could not be observed (Figure 10). This is also consistent with the TG curves (Figure 5) and the calculated constant rates (Table 3). The oxide layers of 16Mo3 and 13Cr are brittle and crumble during sample preparation, which leads to unreliable measurements of the oxide layer thickness, so we focused on the thermogravimetric measurements.

4. Conclusions

This comprehensive study shows the complex phenomena associated with the formation of oxide layers during the high-temperature oxidation of various boiler steels at a uniform temperature of 650 °C. The results and conclusions from this investigation can be summarised as follows:

- The investigation revealed different oxidation behaviour of the steels examined, which underlines the role of the alloy composition. In particular, the steel 16Mo3 showed the highest oxidation rate, followed by 13Cr, T24 and P91. This variation underlines the importance of the alloy composition, especially the presence of chromium, for the oxidation kinetics.
- CALPHAD calculations provided valuable insights into the thermodynamically stable phases that form under different conditions of oxygen activity. The presence of internal oxidation, indicated by stable sublayers beneath the steel surface, underlined the complexity of the development of the oxide layer.
- Thermogravimetric analysis (TGA) shows the kinetics of oxidation for each steel. The different kinetics observed for each steel confirms the influence of composition on the oxidation process. These results are particularly important for understanding high temperature corrosion in practical applications.
- Microscopic examination using SEM and EBSD techniques provided detailed insights into the morphology and composition of the oxide layers. These analyses showed a direct correlation between oxide layer thickness and oxidation kinetics, with 16Mo3 and 13Cr forming the thickest oxide layers. In addition, the EBSD analysis identified the presence of different phases within the oxide layers (hematite and magnetite).
- The results of this study have profound implications for the industry that relies on boiler steels. Understanding the different oxidation behaviour and mechanisms of different steels can help with material selection and corrosion mitigation strategies in high temperature environments.

Author Contributions: Conceptualization, T.B., J.B. and B.Ž.; methodology, T.B. and J.B.; validation, T.B., J.B., B.Š.B. and B.Ž.; investigation, T.B. and B.Š.B.; resources, B.Ž.; writing—original draft preparation, T.B., J.B., B.Š.B. and B.Ž.; writing—review and editing, T.B., J.B. and B.Ž.; visualization, T.B., J.B. and B.Ž. All authors have read and agreed to the published version of the manuscript.

Funding: Funding was provided by the Slovenian Research Agency ARRS program P2-0050 (C).

Conflicts of Interest: The authors declare no conflict of interest.

References

1. Hagarová, M.; Baranová, G.; Fujda, M.; Matvija, M.; Horňak, P.; Bednarčík, J.; Yudina, D. High Temperature Oxidation Behavior of Creep Resistant Steels in Water Vapour Containing Environments. *Materials.* **2022**, 15. doi:10.3390/ma15020616.
2. Sturm, R.; Jenko, M.; Ule, B. a Creep-Properties Evaluation of P91 Steel Weldments Using Short-Term Testing. *Mater. Tehnol.* **2002**, 36, 319–324.
3. Bhadeshia, H. K. D. H. Design of ferritic creep-resistant steels. *ISIJ Int.* **2001**, 41, 626–640. http://cat.inist.fr/?aModele=afficheN&cpsidt=1086338.
4. Toghraee, A.; Zaeem, M. A. Oxidation induced stresses in high-temperature oxidation of steel: A multiphase field study. *Metals.* **2020**, 10, 1–14. doi:10.3390/met10060801.
5. Nguyen, V. P.; Ibupoto, F. A.; Pham, L. Q.; Choi, W.; Shin, K.; Kim, B. J.; Kim, M. K.; Choi, S. T. Creep lifetime prediction of 9Cr-1Mo (grade T91) steel via small punch creep tests and hierarchical multiscale analysis. *Mater. High Temp.* **2020**, *37*, 462–477. doi:10.1080/09603409.2020.1824852.
6. Dudziak, T.; Łukaszewicz, M.; Simms, N.; Nicholls, J. Analysis of High Temperature Steam Oxidation of Superheater Steels Used in Coal Fired Boilers. *Oxid. Met.* **2016**, *85*, 171–187. doi:10.1007/s11085-015-9593-9.
7. Abe, F. Bainitic and martensitic creep-resistant steels. *Curr. Opin. Solid State Mater. Sci.* **2004**, *8*, 305–311, doi:10.1016/j.cossms.2004.12.001
8. Abe, F.; Kern, T.-U.; Visawanathan, R. *Creep-resistant steels*; Abe, F.; Kern, T.-U.; Visawanathan, R., Eds.; Woodhead Publishing and Maney Publishing UK, 2008.
9. P. Klučiar, I. Barenyi, J. Majerík, Nanoindentation Analysis of Inconel 625 Alloy Weld Overlay on 16Mo3 Steel, *Manuf. Technol.* **2022**, 22, 26–33. doi:10.21062/mft.2022.013.
10. M. Gwoździk, M. Motylenko, D. Rafaja, Microstructure changes responsible for the degradation of the 10CrMo9-10 and 13CrMo4-5 steels during long-term operation, *Mater. Res. Express.* **2019**, 7, 0–9. doi:10.1088/2053-1591/ab5fc8.
11. A. Zieliński, G. Golański, M. Sroka, Influence of long-term ageing on the microstructure and mechanical properties of T24 steel, *Mater. Sci. Eng. A*. **2017**, 682, 664–672. doi:10.1016/j.msea.2016.11.087.
12. B. Žužek, F. Vodopivec, B. Podgornik, M. Jenko, M. Godec, Calculation of accelerated stationary creep rate activation energy for a steel microstructure with a uniform distribution of carbide particles, *Mater. Tehnol.* **2012**, 46, 661–664.
13. A. Nagode, L. Kosec, B. Ule, Uni-axial and multi-axial creep behaviour of P91-type steel under constant load, *Eng. Fail. Anal*. **2011**, 18, 61–67. doi:10.1016/j.engfailanal.2010.08.005.
14. A. Nagode, B. Ule, M. Jenko, L. Kosec, A constitutive creep equation for 9Cr Mo-0.2V (P91 -type) steel under constant load and constant stress, *Steel Res. Int.* **2007**, 78, 638–642. doi:10.1002/srin.200706259.
15. Thermo-Calc Software TCOX9 - TCS Metal Oxide Solutions Database 1992, 7.
16. Young, D.J. *High Temperature Oxidation and Corrosion of Metals*; Elsevier: Amsterdam ; Boston ; London, 2008; ISBN 9780080445878.
17. Chen, R.Y.; Yeun, W.Y.D. Review of the High-Temperature Oxidation of Iron and Carbon Steels in Air or Oxygen. *Oxid. Met.* **2003**, 59, 433–468, doi:10.1023/A:1023685905159.
18. Pilling, N.B.; Bedworth, R.E. Oxidation of metals at high temperatures. *J. Inst. Met*. **1923**, 29, 529–539.
19. Kofstad, P. Oxidation of Metals: Determination of Activation Energies. *Nature* **1957**, *179*, 1362–1363, doi:10.1038/1791362a0.
20. Mathiazhagan, P.; Khanna, A.S. High temperature oxidation behavior of P91, P92 and E911 alloy steels in dry and wet atmospheres. *High Temp. Mater. Process.* **2011**, *30*, 43–50, doi:10.1515/HTMP.2011.006.